Journal Pre-proofs

Research Paper

Flow field and heat transfer in the transitional type of turbulent round jet impingement

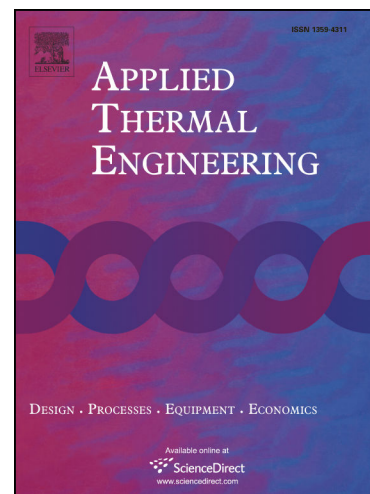Huakun Huang, Jingxuan He, Qingmo Xie, Tiezhi Sun, Guiyong Zhang, Peng Yu

Please cite this article as: H. Huang, J. He, Q. Xie, T. Sun, G. Zhang, P. Yu, Flow field and heat transfer in the transitional type of turbulent round jet impingement, *Applied Thermal Engineering* (2024), doi: https://doi.org/10.1016/j.applthermaleng.2024.124841

Flow field and heat transfer in the transitional type of turbulent round jet impingement

Huakun Huang[1†], Jingxuan He[2†], Qingmo Xie[1], Tiezhi Sun[3], Guiyong Zhang[3, 4], Peng Yu[1, 5*]

[1]Guangdong Provincial Key Laboratory of Turbulence Research and Applications, Department of Mechanics and Aerospace Engineering, Southern University of Science and Technology, Shenzhen, 518055, China

[2]Institute of Intelligent Equipment, Xiamen Tungsten Co., Ltd. Technology Center, Xiamen, 361000, China

[3]State Key Laboratory of Structural Analysis for Industrial Equipment, School of Naval Architecture Engineering, Dalian University of Technology, Dalian 116024, China

[4]Collaborative Innovation Center for Advanced Ship and Deep-Sea Exploration, Shanghai, 200240, China

[5]Center for Complex Flows and Soft Matter Research, Southern University of Science and Technology, Shenzhen, 518055, China

Abstract: Jet impingement heat transfer in the transitional type involves the occurrence and disappearance of the secondary maximum heat transfer, which is challenging for numerical simulation. In the paper, the effects of the nozzle-plate spacing H/D on heat transfer and flow fields in the range of $5 \leq H/D \leq 7$ within the transitional type are investigated. In this type, the secondary maximum heat transfer rate gradually vanishes. In addition, the transitional properties of jet impingement are further discussed. It is found that the heat transfer rate at the stagnation point shows an important relationship with the arriving stream Reynolds number and turbulence intensity. Additionally, three heat transfer modes, i.e., the peak ($5 < H/D \leq 5.5$), swelling ($5.5 < H/D \leq 6.6$), and linear modes ($6.6 < H/D \leq 7$), are identified in the transitional type based on the analysis of the heat transfer rate, development of the intermittency, and the wall shear stress. For the latter two aspects, the laminar zone and the turbulence zone are discussed in detail for different H/D. In the peak mode, heat transfer rate is largely influenced by the transition process, resulting in a secondary peak. While in the swelling mode, the second peak evolves to a swelling and the effect of transition becomes weak. As a result, the influences of the laminar region will extend to downstream. However, in the linear mode, the swelling vanishes with a mild change of intermittency in the boundary layer and the sudden mutation of heat transfer mainly takes place in the stagnation region.

Keywords: Jet impingement; Heat transfer; Second peak; Transitional type; Transition

---

[†]First Author and the Second Author contribute equally to this work

[*]Corresponding Author

1. Introduction

The enhancement of jet impingement heat transfer is a hot topic in academic and industrial areas due to its superior effectiveness in heat and mass transfer over other general single-phase convective heat transfer arrangements [1]. However, jet impingement may induce serious surface heating, ground erosion, and noise problems [2, 3], especially for vertical takeoff and landing aircraft and rockets. Investigating different nozzle-plate spacing H/D and gaining insight into flow and thermal fields become one of the keys to solving the above problems [4]. Here, H is the impinging distance and D denotes the nozzle diameter. In the abovementioned applications, existing studies mainly concentrate on H/D lower than 40 [5–7], particularly for H/D < 10 [8–11]. According to different H/D, jet impingement can be divided into three types, i.e. the small ($H/D < 5.5$), medium ($5.5 \leq H/D \leq 8.3$) and large type ($8.3 < H/D$) based on the analysis of stagnation pressure [12]. However, from the view of heat transfer, the impingement is generally divided into only the small and large types [13]. In different types, the features of heat transfer rate and flow fields are completely different. In the small type, the heat transfer rate exhibits a secondary peak, while this feature gradually vanishes with the increase of H/D [13]. This variation in heat transfer reflects the complex underlying mechanism, causing an obstacle to accurate prediction using turbulence models [1,13,14]. Due to this reason, few studies for the transitional properties of heat transfer and flow fields are reported in the literature. Focusing on the above challenge, the transitional impingement type between the small and large types is investigated in this paper.

Many researchers have attempted to understand the transitional type in depth. When $H/D < 6$, there are two peaks of heat transfer rate. For the first peak, it occurs around the stagnation point due to the interaction of the primary vortex developed from the shear layer in the free-jet region and the impermeable wall. Away from the stagnation point, the heat transfer rate gradually decreases. However, at low H/D, the second vortex can be triggered by the above interaction [15] if the inlet Reynolds number (Re) is high enough. As a result, the heat transfer rate starts to increase at a certain position until the wall jet flow is fully developed. And the secondary maximum of the heat transfer rate is formed. While for higher H/D, the above phenomenon disappears due to the breakdown of the primary vortex before impinging the plate [16]. Consequently, the distribution of heat transfer rate shows a monotonic reduction trend away from the stagnation point [17,18]. Due to the complexity when $H/D < 6$, the cases of $H/D = 2$ with the primary vortex and the second vortex movement are mostly investigated in order to confirm the formation of the second peak of heat transfer [15]. However, the exploration for the second peak of heat transfer remains to be an open topic. For the velocity field, Guo et al. [19] showed the wall jet's development of confined jet impingement with Re ranging from 1,000 to 9,000 at $H/D = 2$, 4, and 8. They found a recirculation core existing at small H/D. The location of the recirculation coincides with the maximum wall jet velocity. After this station, the self-similarity of wall jet is unsatisfactory for $Re = 1000$. At $H/D = 8$ and 4, the wall jet shows a similar performance. However, for turbulent jet impingement, the similarity of the wall jet may be not perfect owing to the influence of turbulence. In addition, the above investigated Reynolds numbers are relatively small, leading to the weak influence of the second vortex at small H/D. Instead of focusing on small H/D, Shademan et al. [20] paid attention to the large types ($H/D = 20$) with $Re = 28,000$ and discovered the

asymmetrical impingement of primary vortex based on the large eddy simulation (LES), which is very different from the axisymmetric behavior in the small type. Zhe and Modi [21] experimentally discussed the change of flow fields for $1 \leq H/D \leq 9$ in terms of the velocity and the skin friction coefficient C_f ($C_f = \tau_w/(0.5\rho U_b^2)$, where τ_w is the wall shear stress, ρ is the density and U_b represents the bulk velocity) for plane jet impingement. For the small type, there is an obvious secondary maximum for C_f which cannot be found in other types. In addition, the profiles of C_f for all types nearly overlap with each other downstream, which seems to be independent on H/D. Cooper et al. [8] and Tummers et al. [22] conducted a series of experiments at $H/D = 2$, 6 and 10 for the round jet impingement in terms of flow fields. Unfortunately, H/D changes in a relatively large step, leading to difficulty in capturing subtle changes of different types. However, these changes are important for understanding the enhancement of the heat transfer rate for different nozzle-plate spacing when designing a product [23].

For heat transfer, Zuckerman and Lior [1] summarized a great number of empirical formulas for jet impingement heat transfer from literature. However, these formulas either are mainly associated with heat transfer at the stagnation point or average heat transfer on the impinging plane. It is difficult to recognize the importance of the transitional region where the secondary peak of heat transfer rate emerges. Huang et al. [24] stated that the heat transfer rate in the transitional region plays an important role in the average heat transfer downstream. The major contribution is mainly due to the secondary peak of heat transfer. However, to accurately estimate the importance of heat transfer rate in the transitional region, one of the challenges is to precisely capture the change of heat transfer rate. As mentioned above, this is because there are two distinct underlying physics. Abraham and Vedula [25] conducted experimental investigations to study the effect of H/D on heat transfer rate for small types. They found that the secondary peak of heat transfer rate is affected by the entrainment. Isman et al. [26] employed the transition shear stress transport model proposed by Langtry and Menter (SSTLM) [27] to investigate the transition properties of heat transfer at a fixed H/D of 4. Unfortunately, they pointed out that none of the laminar-turbulence transition models could capture the exact location of the secondary peak. Using the SSTLM model, Alimohammadi et al. [28] stated that the turbulent intensity Tu at the centerline increases with enhancing H/D, leading to the disappearance of the secondary peak of heat transfer. However, the secondary peak of heat transfer failed to be captured at $H/D = 3$ using the SSTLM model [28]. Considering the limitation of the SSTLM model, only the cases of $H/D = 1, 2, 3, 4$, and 6 are discussed in the work of Alimohammadi et al. [28]. Several researchers [1,29] reviewed many turbulence models' performance in predicting heat transfer for jet impingement. In these works, the SST model and the $v^2 - f$ were recommended for jet impingement due to their fair good ability in predicting the secondary peak of heat transfer. However, although the $v^2 - f$ model performs well in predicting the heat transfer rate and flow fields compared with other RANS models [1,30,31], getting the robust results remains to be difficult due to the non-linear term [32]. Therefore, the SST model are generally used for jet impingement [33–36]. However, the SST model is weak in capturing the second peak of heat transfer [37]. Huang et al. [13,38] proposed a cross-diffusion correction based on the SST model for the round jet impingement at $H/D = 2, 4$, and 6. Good agreements in flow and thermal fields can be observed between simulations and experiments. Yet they mainly focused on the model validation, and thus the transitional properties of jet impingement

95 for H/D were not further studied. In addition, at high H/D, the underestimation of the
96 above model for heat transfer rate can be found in their work, which is due to the
97 increase of dissipation by the cross-diffusion correction [13]. Similar investigations can
98 also be found in the work of Jaramillo et al. [14]. Due to the above reason, jet
99 impingement is recognized as a benchmark flow for examining the predictive accuracy
100 of turbulence models. And the effects of H/D remain to be an important issue for jet
101 impingement [35,38–40].

102 Therefore, from the above analysis, it is clear that the flow and thermal fields in the
103 transitional type have not been understood comprehensively. The main causes are the
104 large H/D step and inaccurate turbulence models adopted for jet impingement. The
105 core problem is that the occurrence and disappearance of the secondary peak of heat
106 transfer are hard to be predicted accurately due to complex phenomena. Even for the
107 experiment, measurements for flow field and heat transfer are also challenging. This is
108 because that many influential factors are associated with the time and space scales.
109 Consequently, many experiments would only aim at either flow field or heat transfer,
110 such as the work of Baughn et al. [9], Cooper et al. [8], and Ahmed et al. [41].
111 Considering the above issue, we would like to use an efficient mathematical tool to
112 achieve the above purpose in this paper. And then, the transitional properties in flow
113 and thermal fields will be studied comprehensively. Based on the investigation, we
114 want to provide some insight into the unresolved questions for the transitional type of
115 round jet impingement, including how the secondary peak of heat transfer rate and the
116 skin friction vary with H/D and how the laminar-turbulence transition influences the
117 heat transfer rate.

118 In the remaining of the paper, the numerical methods including the governing
119 equations, turbulence models, and problem descriptions are described in Sec. 2. Sec. 3
120 presents the results and discussions about the model validation and the transitional
121 properties in terms of heat transfer and flow fields. The primary remarks are provided
122 in Sec. 4.

123 *2. Numerical methods*

124 Although the direct numerical simulation (DNS) and LES have the advantages of
125 predicting flow fields and heat transfer, they require huge computational resources and
126 time. Therefore, a Reynolds-Averaged Navier-Stokes (RANS) turbulence model
127 proposed by Huang et al. [38] is employed due to good performance in capturing the
128 heat transfer characteristics. To reinforce the performance of the above model, the
129 SSTLM model is coupled with the above Huang's model. All codes are based on the
130 open sources library called Field Operation And Manipulation (OpenFOAM) for the
131 version of v2312 [42] to make the coupled method robust and accurate.

132 2.1 Governing equations

133 For the steady-state and incompressible RANS method, the mass, momentum and
134 energy conservation equations in the Cartesian coordinates can be written as

$$\frac{\partial u_i}{\partial x_i} = 0 \tag{1}$$

4

$$\rho u_j \frac{\partial u_i}{\partial x_j} = -\frac{\partial p}{\partial x_i} + \frac{\partial}{\partial x_j}(2\mu S_{ij} - \rho \overline{u'_i u'_j}) \tag{2}$$

$$u_i \frac{\partial \rho T}{\partial x_j} = \frac{\partial}{\partial x_i}\left(\frac{\lambda}{c_p}\frac{\partial T}{\partial x_i} - \rho \overline{u'_i T'}\right) \tag{3}$$

135 where u is the mean velocity, ρ is the density, p represents the mean pressure, μ
136 denotes the dynamic viscosity, $\overline{u'_i u'_j}$ is the Reynolds stress, $\overline{u'_i T'}$ is the turbulent heat
137 flux vector, c_p is the specific heat capacity at the constant pressure, T is the temperature,
138 and S is the rate of strain tensor. For the RANS method, the Reynolds stress and
139 turbulent heat flux vector remain to be unknown, which have to be resolved by
140 turbulence models.

141 2.2 The SST model

142 The SST model is a hybrid method, for which the k-ω model is activated near the
143 wall and the k-ε model is used for the free shear flows [43]. Here, ω is the specific
144 dissipation rate, and the ε is the dissipation rate. As mentioned before, this model has
145 been widely used for various jet impingement problems due to its fairly good
146 performance. This is why a large number of developed approaches are based on the
147 SST model, as mentioned in Introduction. In this model, the eddy viscosity μ_t, turbulent
148 kinetic energy k, and the specific dissipation rate ω have the following forms

149 Eddy viscosity:

$$\mu_t = \frac{\rho a_1 k}{\max(a_1 \omega, SF_2)} \tag{4}$$

150 Turbulent kinetic energy：

$$\frac{\partial(\rho u_j k)}{\partial x_j} = \tilde{P}_k - \beta^* \rho k \omega + \frac{\partial}{\partial x_j}[(\mu + \mu_t \sigma_k)\frac{\partial k}{\partial x_j}] \tag{5}$$

151 Specific dissipation rate：

$$\frac{\partial(\rho u_j \omega)}{\partial x_j} = \alpha \rho S^2 - \beta \rho \omega^2 + \frac{\partial}{\partial x_j}\left[(\mu + \mu_t \sigma_\omega)\frac{\partial \omega}{\partial x_j}\right] + 2(1-F_1)\rho \sigma_{\omega 2}\frac{1}{\omega}\frac{\partial k}{\partial x_j}\frac{\partial \omega}{\partial x_j} \tag{6}$$

152 where turbulent kinetic energy production term $\tilde{P}_k$ can be written as

5

$$P_k = \mu_t \frac{\partial u_i}{\partial x_j} \left(\frac{\partial u_i}{\partial x_j} + \frac{\partial u_j}{\partial x_i} \right) \tag{7}$$

$$\tilde{P}_k = \min(P_k, 10\beta^* \rho k \omega) \tag{8}$$

153 The blending functions F_1 in Eq. (6) and F_2 in Eq. (4) are defined as

$$F_1 = \tanh \left\{ \left\{ \min \left[\max \left(\frac{\sqrt{k}}{\beta^* \omega y}, \frac{500v}{y^2 \omega} \right), \frac{4\rho \sigma_{\omega 2} k}{CD_{k\omega} y^2} \right] \right\}^4 \right\} \tag{9}$$

$$F_2 = \tanh \left[\left[\max \left(\frac{2\sqrt{k}}{\beta^* \omega y}, \frac{500v}{y^2 \omega} \right) \right]^2 \right] \tag{10}$$

$$CD_{k\omega} = \max(2\rho \sigma_{\omega 2} \frac{1}{\omega} \frac{\partial k}{\partial x_j} \frac{\partial \omega}{\partial x_j}, 10^{-10}) \tag{11}$$

154 where $v = \mu/\rho$. Therefore, F_1 and F_2 keep unity near the wall and become zero in the
155 free shear flows. The turbulence closure coefficients are $\sigma_k = F_1 \sigma_{k1} + (1 - F_1)\sigma_{k2}$, σ_{k1}
156 $= 0.85$, $\sigma_{k2} = 1$, $\sigma_\omega = F_1 \sigma_{\omega 1} + (1 - F_1)\sigma_{\omega 2}$, $\sigma_{\omega 1} = 0.5$, $\sigma_{\omega 2} = 0.856$, $\alpha = F_1 \alpha_1 + (1 - F_1)\alpha_2$, $\alpha_1 = 5/9$, $\alpha_2 = 0.44$, $\beta = F_1 \beta_1 + (1 - F_1)\beta_2$, $\beta_1 = 0.075$, $\beta_2 = 0.0828$, and β^*
158 $= 0.09$.

159 2.3 The transition model

160 In this work, the SSTLM model coupled with the SST model with the cross-diffusion
161 correction (CD) developed by Huang et al. [38] (SSTCDLM) is used. Additionally, the
162 vortex stretching correction in the work of Huang et al. [17] is also added for
163 reproducing the accurate flow fields. As mentioned above, the SSTLM model shows
164 superior performance in capturing the second peak of heat transfer, which can also be
165 found in the paper. However, it easily reproduces a false second peak of heat transfer
166 at high H/D, especially for plane jet impingement. By introducing the cross-diffusion
167 and vortex stretching corrections, the SSTCD model gives a monotonic reduction of
168 heat transfer at high H/D, which shows a better performance than that of the SSTLM
169 model. However, heat transfer rate is underpredicted downstream by the SSTCD model,
170 while it can be captured well by the SSTLM model in the same region. To take the
171 advantage of both models, the transport equations of the turbulent kinetic energy k and
172 the specific dissipation rate ω are modified as follows

$$\frac{\partial(\rho u_j k)}{\partial x_j} = \min(\gamma_{eff} P_k, 10\rho \beta^* k \omega) - D_k + \frac{\partial}{\partial x_j} \left[(\mu + \mu_t \sigma_k) \frac{\partial k}{\partial x_j} \right], P_k = \mu_t S\Omega \tag{12}$$

$$\frac{\partial(\rho u_j \omega)}{\partial x_j} = \alpha \rho S^2 - \beta \rho \omega^2 + \frac{\partial}{\partial x_j}\left((\mu + \mu_t \sigma_\omega)\frac{\partial \omega}{\partial x_j}\right) + 2(1-F_1)\rho\frac{\sigma_{\omega 2}}{\omega}\frac{\partial k}{\partial x_j}\frac{\partial \omega}{\partial x_j} \quad (13)$$

173 Using the cross-diffusion and vortex stretching corrections of Huang et al. [17,38], the
174 destruction term D_k in Eq. (12) can be rewritten by

$$D_k = \min\bigl(\max(\gamma_{eff}, 0.1), 1.0\bigr)\tilde{\beta}^* \rho k \omega \quad (14)$$

175 where γ_{eff} is the effective intermittency, $\tilde{\beta}^*$ is the modified cross-diffusion correction,
176 and β in Eq. (13) has to be rewritten based on the vortex stretching correction. Finally,
177 the parameters of $\tilde{\beta}^*$ and β have the following forms

$$\tilde{\beta}^* = F_1 \beta_1^* + (1-F_1)\beta_2^*, \beta_1^* \quad (15)$$
$$= 0.08\frac{1 + 680\chi_k^2}{1 + 400\chi_k^2}, \beta_2^*$$
$$= 0.09, \chi_k = \frac{1}{\omega^3}\frac{\partial k}{\partial x_j}\frac{\partial \omega}{\partial x_j}$$

$$\beta = F_1 \beta_1 + (1-F_1)\beta_2, \ \beta_1 = 0.075, \beta_2 \quad (16)$$
$$= \frac{1 + 90\chi_\omega}{1 + 100\chi_\omega}\cdot 0.0828$$

178 where χ_ω is the stretching factor. It should be noted that the turbulence constants in the
179 formulation of β_1^* are different from the previous works. In the SSTCDLM model, the
180 intermittency γ and the transition momentum-thickness Reynolds number $\widetilde{Re}_{\theta t}$ can be
181 resolved as following

$$\frac{\partial \rho u_j \gamma}{\partial x_j} = P_\gamma - E_\gamma + \frac{\partial}{\partial x_j}\left[\left(\mu + \frac{\mu_t}{\sigma_f}\right)\frac{\partial \gamma}{\partial x_j}\right] \quad (17)$$

$$\frac{\partial \rho u_j \widetilde{Re}_{\theta t}}{\partial x_j} = P_{\theta t} + \frac{\partial}{\partial x_j}\left[\sigma_{\theta t}(\mu + \mu_t)\frac{\partial \widetilde{Re}_{\theta t}}{\partial x_j}\right] \quad (18)$$

182 where P_γ, E_γ and σ_f are the transition production term, destruction term and constant
183 value of 1.0, respectively. $P_{\theta t}$ is the production term of $\widetilde{Re}_{\theta t}$, $\sigma_{\theta t}$ is equal to 2.0.

184 2.4 Boundary conditions and solution schemes

185 Figure 1 (a) shows the computational domain and boundary conditions for two-
186 dimensional axisymmetric turbulent round jet impingement for the single-phase air

flow. The jet firstly evolves in a long pipe with a length of $70D$ as shown in Figure 1 (b). At the nozzle inlet, a uniform velocity U_D is imposed based on $Re = 23{,}000$ if not specifically pointing out. Under this condition, the turbulent intensity Tu is 4.5%. The turbulent kinetic energy k is set by $k = 1.5(U_D Tu)^2$, and the specific dissipation rate ω $= \sqrt{k}/(0.015D \cdot 0.09^{0.25})$. After the flow fully develops in the pipe, the velocity u_{in}, the turbulent kinetic energy k_{in}, and the specific dissipation rate ω_{in} at the nozzle outlet are prescribed to the inlet for the round jet impingement. At the outlet, the pressure is kept the same with the ambient pressure of 10,1325 Pa, while the other variables' normal gradient to the outlet is considered zero. For the heated wall, a no-slip wall with a constant temperature $T_w = 318\,\text{K}$ boundary condition is used. The ambient temperature is the same as the inlet temperature $T_{in} = 298$ K. For the pipe wall, a no-slip and adiabatic wall condition is applied. At each wall boundary, the turbulent kinetic energy k is equal to a very small value of 1×10^{-8}, and the specific dissipation rate ω is evaluated using the omega wall function designing for low- and high-Re flows. For the pressure inlet, the zero turbulence and $5\%U_D$ of velocity are considered. It should be noted that the above boundary conditions will be kept the same for all the cases in the paper for studying the transitional properties of jet impingement.

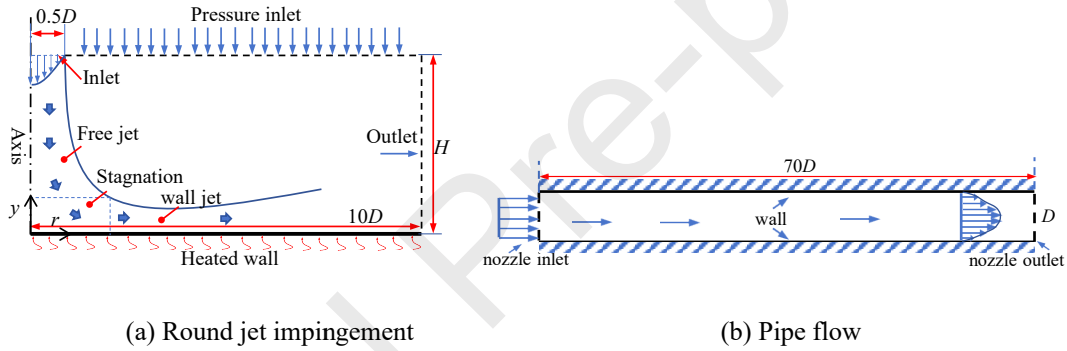| (a) Round jet impingement | (b) Pipe flow |

Figure 1. Computational domain and boundary conditions

The two-dimensional steady-state conservation equations are discretized using the finite volume method (FVM). The velocity-pressure coupling is resolved by the Semi-implicit Method for Pressure-linked Equation (SIMPLE) approach. The velocity and turbulence are discretized using the second-order upwind scheme to improve the predicted accuracy. To avoid the computational instability, the gradient scheme "faceMDLimited" in OpenFOAM is adopted for the pressure and velocity, while the "faceLimited" is used for turbulence. The interpolation scheme is the second-order "Gauss linear corrected" method. The residuals for momentum and turbulence equations are 1×10^{-4}. As for the energy, a residual value of 1×10^{-6} is considered. Therefore, in each case, when all variables' residuals are lower than the above criteria, the solution will be treated as convergent and thus the simulation is stopped.

2.5 Validation of grid independence

The hexahedral, structured grid topology shown in Figure 2 is generated using the application of blockMesh in OpenFOAM. In this platform, it should be noted that a wedge-shape geometry must be built in order to simulate the axisymmetric simulation, as shown in Figure 2 (a). For this wedge shape, the rotation angle should be lower than 5 degrees. In addition, the boundary of the axisymmetric wedge plane has to be set as

224   wedge type. For the refinement region, it is near the impinging plane and the line $r/D =$

225   0.5 to well predict the effect of viscosity and development of the shear layer,

226   respectively. To investigate the grid independence, the cases of $H/D = 2$ and 6 are

227   carried out, which are also used in the subsequent model validations in Subsec. 3.1.

228   Three grid resolutions, i.e., grid1, grid2, and grid3, are employed for each case, for

229   which the total number of cells in the r and y directions are n_r and n_y, respectively. For

230   the case of $H/D = 2$, the cell numbers for the three grids are 126×100, 190×120,

231   and 350×144, respectively. As for the case of $H/D = 6$, the corresponding cell

232   numbers for the three grids are 147×100, 210×140, and 368×160, respectively. In

233   addition, since the current flows belong to the low-Re flow, meaning that the viscosity

234   effect is very important. Thus, the first grid distance to the wall should be located within

235   the viscous sublayer, for which a recommended y^+ ($y^+ = y\sqrt{\tau_w \rho}/\mu$) should be lower
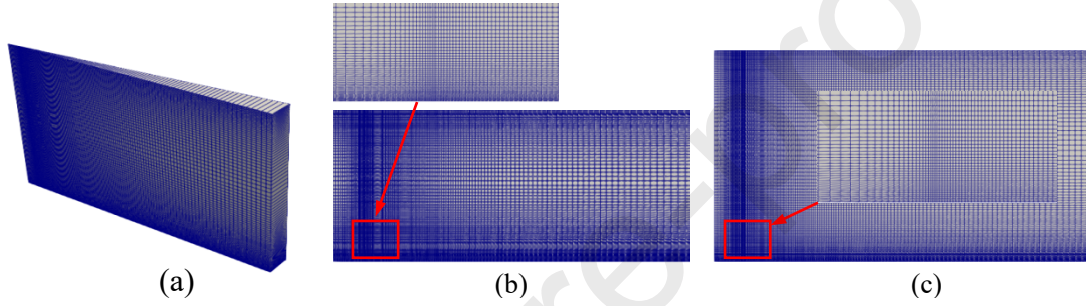
236   than 2.5 [13,14] for all the grid schemes.

237

238 Figure 2. Sample grids. (a) The side view, (b) the front view for H/D=2, and (c) the front view for

239 H/D=6

240   It is to be noted that for convenience, the numerical results of the paper will be

241   extracted in a cutting plate that is parallel with the r-y plane. Figure 3 presents profiles

242   of the non-dimensional parameter Nu along the impinging plane for different grid

243   schemes using the SSTCDLM model. Here, Nu can be defined by $Nu = hD/\lambda$, where h

244   is the heat transfer coefficient and λ denotes the fluid thermal conductivity. h can be

245   further extracted by $h = -\lambda \frac{\partial T}{\partial y}\big|_w /(T_w - T_{in})$. In Figure 3 (a), it can be found that the

246   maximum error between the results of grid1 and grid2 is found around $r/D = 2.1$ for $H/$

247      $D = 2$, which is about 4.3%. For the results of grid2 and grid3, the deviations between

248   them are much smaller than those of grid1 and grid2 in the same location. As a result,

249   it can be drawn that the results of grid2 are independent of grids which is fine enough

250   in this investigation. As for the case of $H/D = 6$, the maximum deviation occurs around

251      $r/D = 2$ and the stagnation point ($r/D = 0$) among the results of three grids. The results

252   of grid1 show the highest first peak and the secondary peak of Nu, which depart from

253   the results of the other two grids obviously. While the results of grid2 and grid3 almost

254   overlap along the whole plane, showing good convergent features. Thus, for the case of

255      $H/D = 6$, grid2 is also considered as the convergent grid resolution. Moreover, the

256   above similar conclusions can be also drawn from the profiles of the velocity magnitude

257   U_{mag} at $r/D = 2$ for different cases, as depicted in Figure 4. Figure 5 further shows the

258   distributions of y^+ for different cases over the plane. It can be found that, the values of

259   y^+ in Figure 5 for both cases are lower than 2.5, satisfying the above criteria. For this

260   reason, grid2 for both cases is used for the subsequent study. Using the above

261   approaches, the investigation of grid independence is also done for other cases

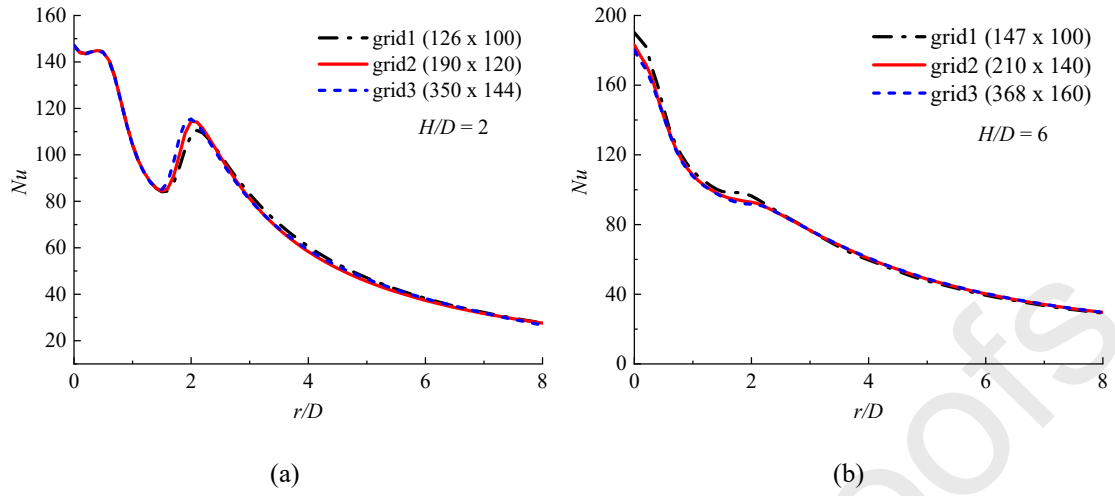262 mentioned in the paper, which is not shown here.

263

264   (a)   (b)

265 Figure 3. Local Nu along the impinging plane at different grid resolution. (a) $H/D = 2$ and (b) H/D
266   = 6

267

268   (a)   (b)
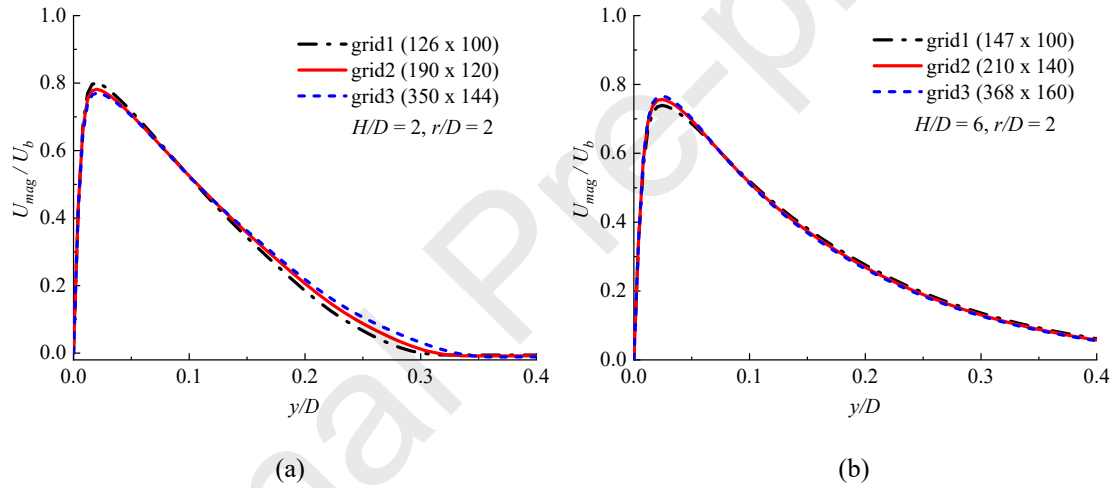
269 Figure 4. Profiles of the velocity magnitude U_{mag} at $r/D = 2$. (a) $H/D = 2$ and (b) $H/D = 6$

270

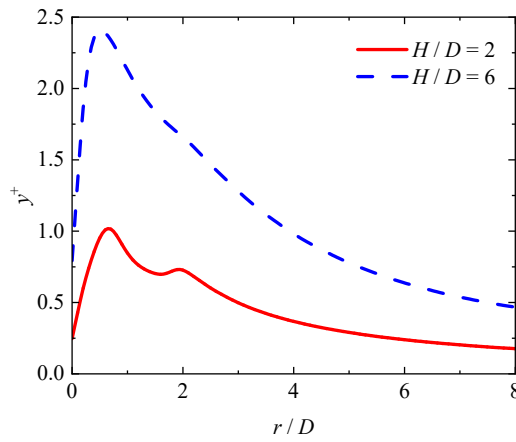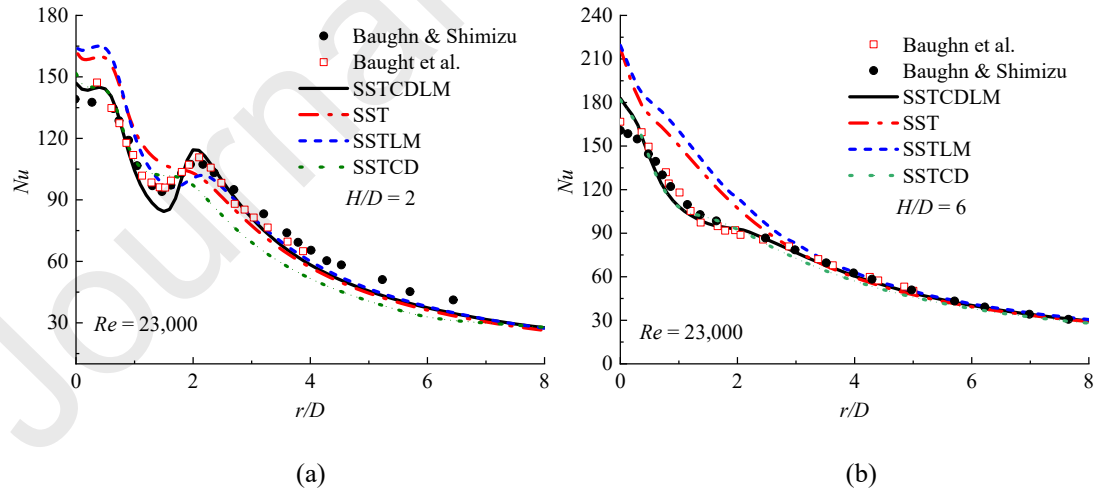271   Figure 5. Profiles of y^+ along the plane for different cases based on the grid2

3. Results and discussions

In this section, the focus is mainly on the transitional properties at $5 \leq H/D \leq 7$ in terms of flow and thermal fields. For this purpose, different models are investigated at low and high H/D and Reynolds numbers. Other boundary conditions are the same for all the cases, which can be found in Sec. 2.4. Based on the well-evaluated model, the transitional features, such as heat transfer rate, the laminar-turbulence transition process, the velocity field, and the skin friction, are further studied under the similar boundary conditions. The details are as follows.

3.1 Validation of turbulence model

In order to evaluate the model's performance in predicting jet impingement, four nozzle-plate spacings are chosen here for H/D = 2, 6, and 10 with Re = 23,000 and 70,000, covering small, transitional, and large imping types. Despite the SST and the SSTCD model being estimated in the previous studies [33,35,39], validations are still conducted to compare the results predicted by these models with the experimental data under the same conditions. As depicted in Figure 6 (a) at H/D = 2, it can be observed that the SST model fails to regenerate the dip and the second peak of Nu, while the SSTLM model gives an accurate dip for both the position and value. As for the SSTCD model, it provides too low energy downstream. This is associated with the addition of cross-diffusion correction activated near the wall, resulting in an increase of dissipation [13]. Adding the transition correction in the SSTCD model, the maximum relative error of the SSTCDLM model is 9.72% compared with the measurement around the dip. Meanwhile, the accuracy for capturing the secondary peak of Nu for the SSTCDLM model is improved by 4.6% over the results of the SSTLM model. Importantly, the underprediction of the SSTCD model is avoided downstream for the SSTCDLM model by adding the transition model.
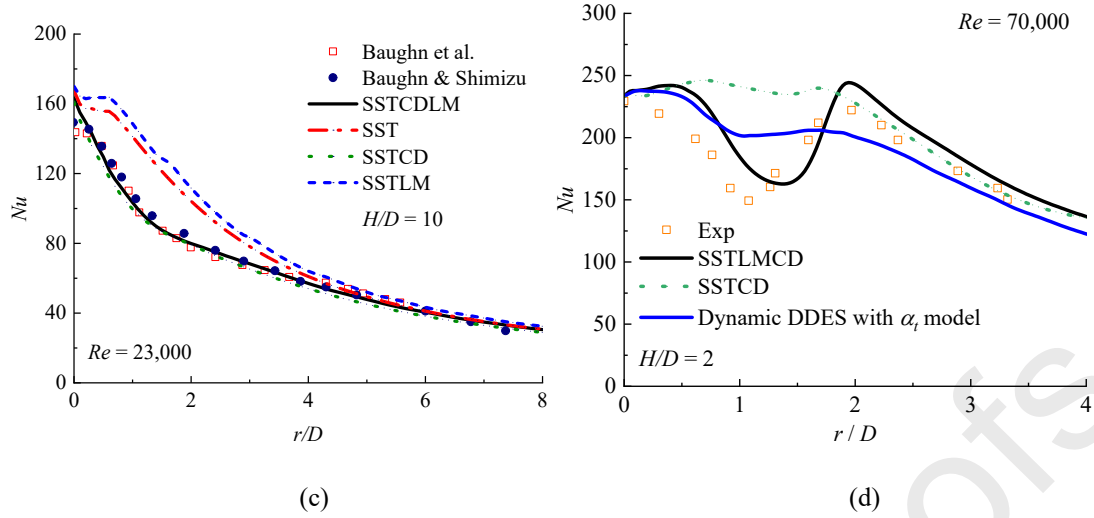

(a)   (b)

11

299

300 (c) (d)

301 Figure 6. Profiles of Nu along the impinging plane for different models compared with the
302 experimental data of Baughn et al. [9], and Baughn and Shimizu [44] (a) $H/D = 2$ (b) $H/D = 6$; (c)
303 $H/D = 10$; (d) $H/D = 2$ with $Re = 70,000$; the scatter is obtained from the experiment [45]

304 The predictions of heat transfer rate for different models for the medium type are
305 shown in Figure 6 (b). The results of the SSTCDLM model match well with the
306 measurements, especially the swelling point around $r/D = 2$. In this impinging type, it
307 should be emphasized that the transition model plays a minor role, leading to small
308 deviations between models with and without the consideration of the laminar-
309 turbulence transition. Unfortunately, the results predicted by the SSTLM and SST
310 models are not only higher than the experimental data but also depart from the trend of
311 Nu for $r/D < 3$ apparently. In the large type in Figure 6 (c), the SSTCDLM model still
312 performs superior. The effect of laminar-turbulence transition increases with $Re =$
313 70,000 in Figure 6 (d), and the SSTCDLM model also demonstrates the good
314 performance. However, the SSTCD model cannot reproduce the dip to reflect the
315 underlying physics for this case. Even for the LES/RANS method, i.e., the dynamic
316 DDES with α_t model [46], it overestimates the heat transfer rate around the dip.
317 Therefore, in the previous studies, it is difficult to study the transitional impinging type.
318 But it becomes possible for us to gain insight into the above issue using the SSTCDLM
319 model.

320 In addition, the accuracy of predicted behavior in the flow fields is another concern
321 for a turbulence model. Figure 7 further provides the results of the SSTCDLM model
322 in velocity magnitude U_{mag} along the y direction at different r/D for cases of $H/D = 2$
323 and 6. At $H/D = 2$, the profiles of U_{mag} predicted by the SSTLM model and the
324 SSTCDLM model show similarly to each other at all locations. However, the profiles
325 for the SSTCDLM model coordinate well with the experimental data [8] at $H/D = 6$,
326 which avoids the underprediction of the velocity peak found for the SSTLM model. As
327 for the SST model, it is not shown here since it performs similarly to the SSTLM model,
328 which is reflected in Figure 6 (b). Due to the same reason, the results of the SSTCD
329 model are also not repeated in Figure 7.
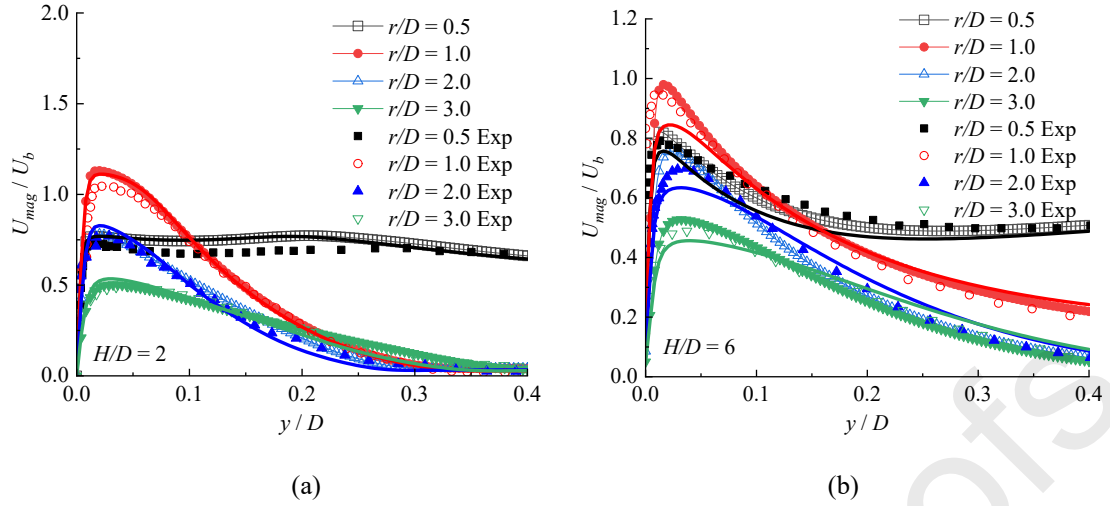
12

(a)

(b)

Figure 7. The comparisons of profiles of the velocity magnitude U_{mag} along the y direction for different locations among the results of the SSTCDLM model, the SSTLM model, and the experimental data [8] (The solid line: the SSTLM model, the solid line with markers: the SSTCDLM model). (a) $H/D = 2$; (b) $H/D = 6$

Therefore, considering the performance in predicting heat transfer rate and velocity field for the small, medium, and large imping types, it is worth stressing that the SSTCDLM model outperforms the SSTCD and other two referred models, which is desired for investigating the transition properties in the transitional imping type.

3.2 The change of heat transfer rate

With the well-evaluated model in hand, Figure 8 shows the Nu contours for $5 \le H/D \le 7$ with $\Delta H/D = 0.1$. There are two areas to be noted, i.e., the region around the stagnation point and the range of $1 \le r/D \le 3$. To exactly illustrate the change, Figure 9 further quantitatively gives the profiles of Nu with $\Delta H/D = 0.2$.

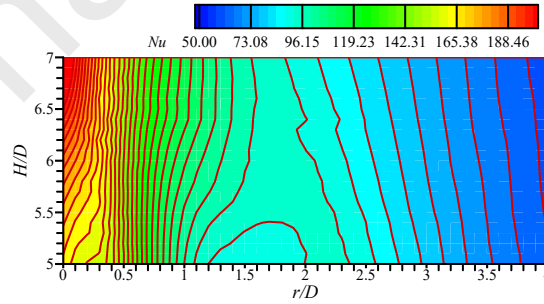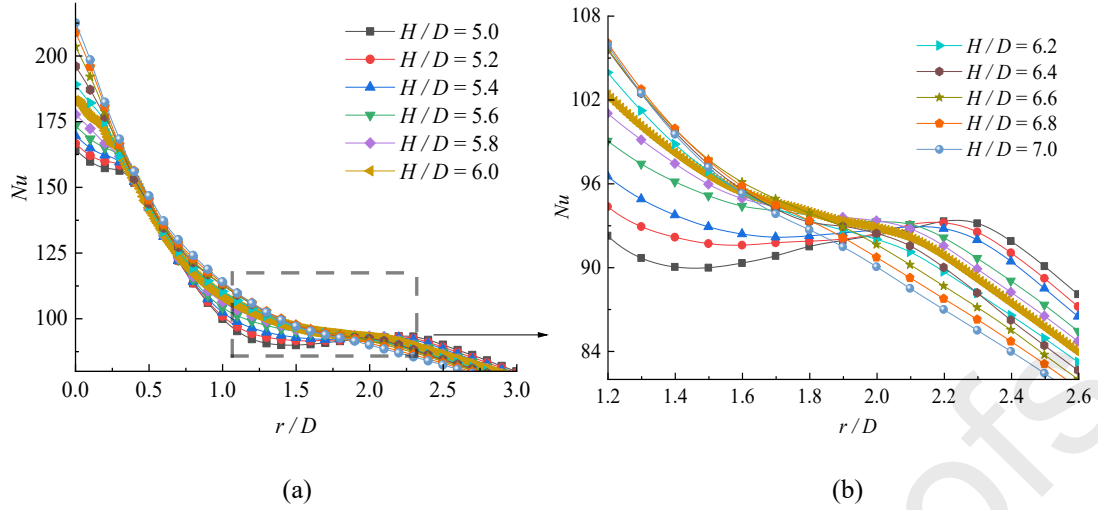Figure 8. Profiles of Nu over the imping plate for $5 \le H/D \le 7$ with $\Delta H/D = 0.1$.

13

348

349   (a)   (b)

350 Figure 9. Profiles of Nu along the impinging plate for different H/D. (a) the whole view and (b) the
351 enlarged view

352   First focusing on the stagnation point, it can be found in Figure 8 and Figure 9 (a)
353 that the stagnation Nusselt number Nu_0 increases with H/D, for which the details are
354 presented in Figure 10 (a). Lee et al. [47] reported the above similar observation and
355 found that both Nu_0 and turbulent intensity Tu ($Tu = \sqrt{2/3k}/U_b$) reach the maximum
356 value synchronously. However, when Nu_0 grows to its maximum value at $H/D = 7$
357 (data are not presented after $H/D = 7$), the turbulent intensity Tu does not reach the
358 maximum yet. This is because the augmentation of the turbulent intensity Tu will be
359 continued until the potential core is fully developed. The end of the potential core can
360 be characterized by the position where the axial velocity equals 95% of the centerline
361 velocity U_{c0} at the nozzle exit. Figure 10 (b) shows the decay of the axial velocity along
362 the centerline for the case of $H/D = 14$. At this high impinging distance, it can be
363 found that the length of the fully developed potential core is $6D$ away from the nozzle
364 exit, which fits well with the experimental data of the free jet at similar conditions [41].
365 Thus, it is clear that when $H/D = 7$, the potential core length is shorter than $(H-y)/D$
366 $= 6$, considering the effect of the wall. In this scenario, Tu should increase beyond H
367 $/D = 7$. However, higher H/D will induce more active jet mixing, resulting in a
368 smaller pressure coefficient C_{p0} at the stagnation point (Figure 10 (a)). Hoogendoorn
369 [48] proposed an empirical function for turbulence round jet impingement over the
370 plane as follows

$$Nu_0/\sqrt{Re_m} = 0.65 + 2.03\left(\frac{TuRe_m^{1/2}}{100}\right) - 2.46\left(\frac{TuRe_m^{1/2}}{100}\right)^2 \qquad (19)$$

371 where m represents properties at the centerline of the free jet, and Tu is obtained at $0.3D$
372 upstream of the stagnation point. Kataoka et al. [49] corrected Eq. (19) for the jet
373 impingement over a flat plate for $2 \leq H/D \leq 10$ with $7{,}000 \leq Re \leq 50{,}000$, which is
374 defined by

$$Nu_0 / \sqrt{Re_m Pr} = 0.78 + 2.43 \left(\frac{Tu Re_m^{1/2}}{100} \right) - 2.94 \left(\frac{Tu Re_m^{1/2}}{100} \right)^2 \qquad (20)$$

where Pr is the Prandtl number. The above two equations are based on the theoretical value of Nu_0 for the turbulence-free condition, which has a simple form $Nu_0 / \sqrt{Re_s Pr}$ = 0.88 [49]. Here, s represents the arriving stream up to $y/D = 0.3$. In this paper, Nu_0 $/ \sqrt{Re_s Pr}$ is within the range of 0.6~0.7. Therefore, considering the effect of Tu, it is found that the following equation fits well with the current results as shown in Figure 10 (a)

$$Nu_0 / \left(2 \times (10Tu)^{1/5} \sqrt{Re_s Pr} \right) \approx 0.036 \qquad (21)$$

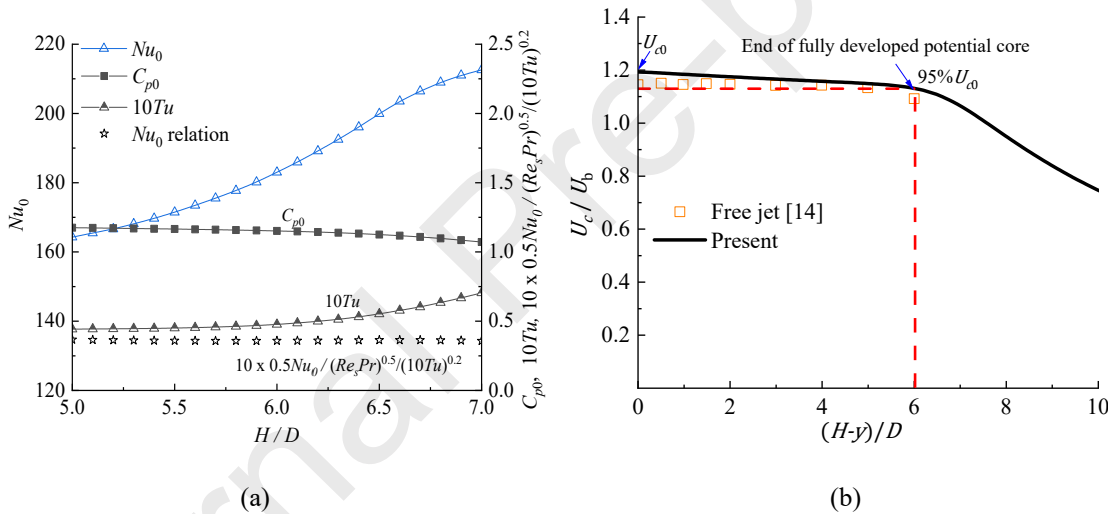(a)   (b)

Figure 10. (a) Pressure coefficient C_{p0} at the stagnation point, turbulent intensity T_u at $y/D = 0.3$, the stagnation Nusselt number (Nu_0) at different H/D, and the current proposed relation for Nu_0; (b) The decay of centerline velocity U_c along the axis at $H/D = 14$ compared with the similar experiment [50]

The local maximum Nu in the range of $1 \le r/D \le 3$ has been received much attention. It is obviously observed in Figure 9 (b) that the local maximum Nu gradually disappears. For convenience, it can be divided into three modes, i.e., the peak, the swelling, and the linear mode. For the peak mode, when $5 \le H/D \le 5.5$, the local maximum and the dip locate around $r/D = 2$ very evidently, as observed in Figure 11. This is because the contour line for the value of zero only takes place for the radial gradient of Nu when $5.5 > H/D$. In this height range depicted in Figure 10 (a), the turbulent intensity Tu is lower than 4.5%, which is possible to trigger the laminar-turbulence transition downstream. Importantly, the present critical value of $H/D = 5.5$ coincides with that proposed by Beltaos and Rajaratnam [12]. Paying attention to Figure 11 again, within the range of H/D from 5.5 to 6.6, the radial gradient of Nu dramatically reduces after $r/D = 2$. Therefore, a swelling appears around $r/D = 2$, as

15

399 depicted in Figure 9 (b). In this mode, the turbulence intensity *Tu* grows from 4.5% to
400 5.78% in the range of $5.5 < H/D \leq 6.6$. In this high turbulence level, the influence of
401 laminar-turbulence transition is weak, resulting in a monotonic reduction in the heat
402 transfer rate in the whole wall jet region. Beyond $H/D = 6.6$, the steep slope in the
403 swelling mode vanishes, leading to the disappearance of swelling. Thus, this regime
404 can be called the linear mode, which represents the change of *Nu* without any swelling
405 or peak. In this stage, the turbulence intensity *Tu* sharply increases to a value larger than
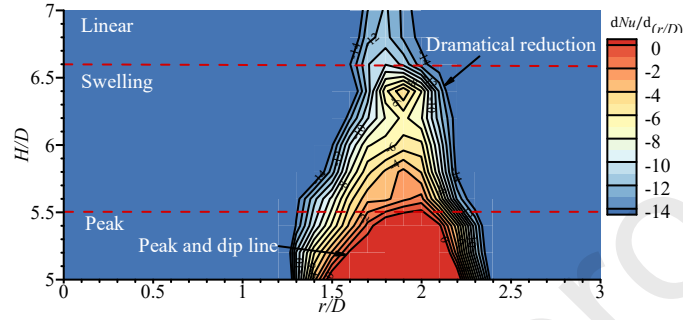406 6%, as shown in Figure 10 (a).

407

408 Figure 11. Radial gradient of *Nu* for different impinging distances

409 Figure 12 provides the average Nusselt number Nu_{avg} along the plate for different
410 impinging distances to further understand what happens during the transition from one
411 mode to another. The definition of Nu_{avg} is written by

$$Nu_{avg} = \frac{1}{r} \int_0^r Nu(r)\, dr \tag{22}$$

412 Nu_{avg} for the three nozzle-plate spacings are chosen to compare with the empirical
413 formulation proposed by Tawfek [51], as depicted in Figure 12 (a). Tawfek's
414 formulation is defined by

$$\begin{aligned}2Nu_{avg}\\= 0.453 Pr^{1/3}(Re)^{0.691}(H/D)^{-0.22}(r/D)^{-0}\end{aligned} \tag{23}$$

415 Notably, the above equation is valid when $2 \leq r/D \leq 30, 6 \leq H/D \leq 58$, and $3,400$
416 $\leq Re \leq 41,000$. Near the stagnation region, the data obtained by the empirical
417 function deviate far from the present results, as shown in Figure 12 (a). Another
418 important point is that for the whole impinging plate, the present Nu_{avg} gradually
419 matches well with the empirical results. This further validates the present numerical
420 model.

421

422   (a)   (b)
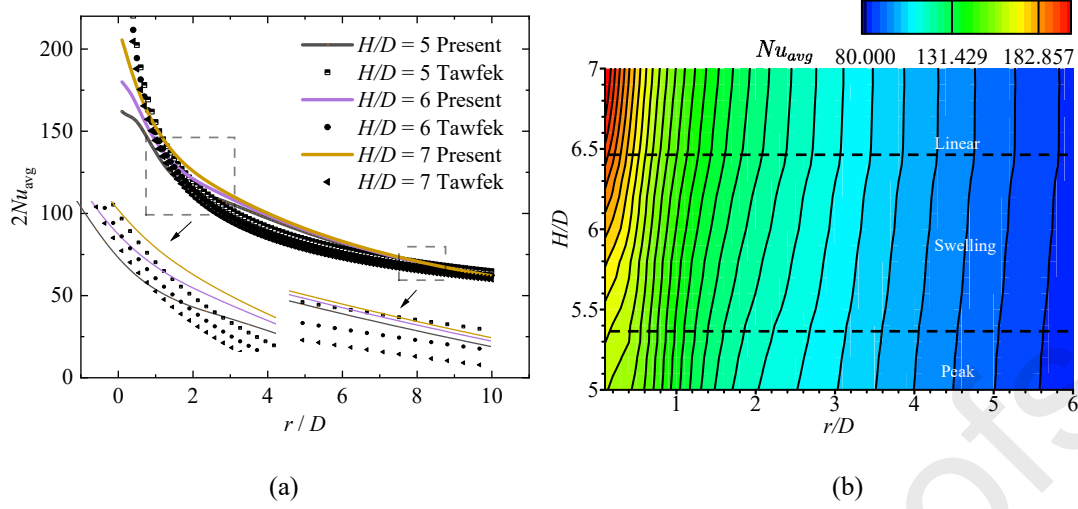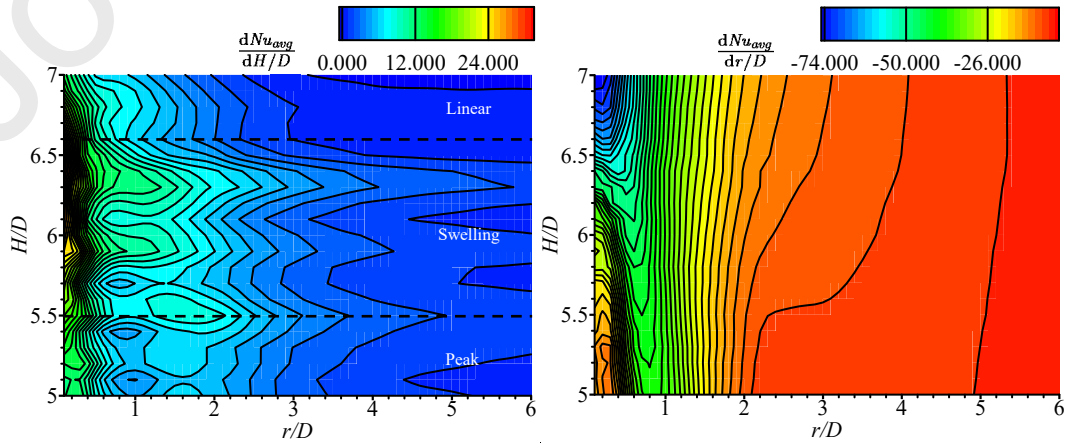
Figure 12. Average Nusselt number Nu_{avg}. (a) Comparisons with the empirical formulation proposed
by Tawfek [51]; (b) Distributions for different nozzle-plate spacing

In Figure 12 (b), Nu_{avg} for all cases are presented using a contour map to illustrate
the subtle changes. In the linear mode, Nu_{avg} is almost parallel for different H/D at
each radial location in the transitional region and downstream. In this mode, the Nu_{avg}
gradient for H/D ($dNu_{avg}/d(H/D)$) depicted in Figure 13 (a) further confirms the
above observation. In the radial direction, the linear behavior is found in the whole plate
shown in Figure 13 (b) in the linear mode where the absolute gradient of Nu_{avg}
decreases uniformly. For the swelling mode, $dNu_{avg}/d(H/D)$ is higher than those in
the other two modes around $r/D = 2$, as shown in Figure 13 (a). As a result, the heat
transfer enhancement is significant even though a small mutation of H/D, particularly
near the boundary of swelling mode. Additionally, the uniformity of Nu_{avg} diminishes
around the stagnation point at higher nozzle-plate spacing (Figure 12 (b) and 13 (b)).
Away from the stagnation point, Nu_{avg} mutates severely in the range of $0.4 < r/D <$
1. Out of this region, the uniformity of Nu_{avg} increases radially in the swelling mode.
In the peak mode, due to small turbulent intensity, Nu_{avg} shows fairly small differences
in the transitional region and downstream when varying H/D. In the radial direction,
there is also a high absolute Nu_{avg} gradient in the region of $0.4 < r/D < 1$, reflecting
an abrupt descent for Nu_{avg}, as shown in Figure 12 (a) and Figure 13 (b). After $r/D =$
2.15, the variation of Nu is very gentle in the peak mode.

443

444   (a)   (b)

445   Figure 13. Average Nusselt number Nu_{avg} gradient in (a) vertical direction and (b) radial direction

446   To understand the behind causes for the above sudden changes, Figure 14 provides
447 the turbulence intensity Tu along the r direction $y/D = 0.025$ for different H/D in
448 detail, which can well reflect the Nu distributions along the impinging plane. For the
449 peak mode, the highest Tu takes place around $r/D = 2$. Therefore, the local maximum
450 peak of Nu is easily observed in the same place. At $H/D = 5.5$, another local maximum
451 peak is formed around $r/D = 1.2$ where the maximum radial velocity takes place. As
452 a result, the gradient of Nu_{avg} over H/D, of course, significantly augments. For the
453 swelling mode, the maximum of Tu gradually moves towards the stagnation region.
454 This movement is influenced by the wall shear stresses and the turbulence level around
455 the stagnation point. As analysis before, for the swelling mode, turbulent intensity Tu
456 is within the range of $4.5\% \leq Tu \leq 5.78\%$, which is higher than that in the peak mode.
457 Therefore, with the help of wall shear stresses, the energy peak of swelling mode occurs
458 around $r/D = 1,$ which is near the maximum wall shear stresses (Figure 17 (b)). In this
459 location, the value of Tu is as high as that in the peak mode. For this reason, the effect
460 of the laminar-turbulence transition is weaker than that in the peak mode. Using the
461 above similar analysis, it is also concluded that the laminar-turbulence transition is
462 difficult to be triggered in the linear mode, leading to no secondary peak or swelling
463 around $r/D = 1.2$.
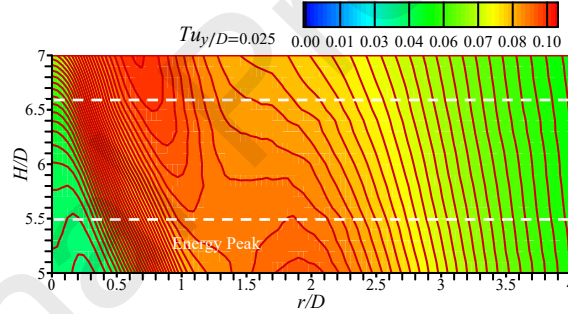
464

465   Figure 14. Distributions of Tu for different H/D.

466 3.3 Transitional characteristics of flow fields

467   The above analysis shows that the flow behaviors in the transitional region have
468 different modes, which are strongly associated with the laminar-turbulence transition.
469 It is well-known that for jet impingement, the flow is in the quasi-laminar state in the
470 stagnation region but becomes turbulent downstream. Focusing on this point, the
471 development of the intermittency γ is extracted in the boundary layer, as shown in
472 Figure 15. The boundary layer thickness δ is defined by the vertical location y where
473 the radial velocity reaches its maximum velocity U_e. It can be observed that the fully
474 developed distance y_f where γ develops from zero to unity away from the wall is not the
475 same in the quasi-laminar region. However, y_f gradually tends to an identical value
476 downstream, showing that the flow is in a turbulent state. Therefore, the development
477 of the intermittency γ in the boundary layer along the impinging plate is consistent with
478 the flow physics of jet impingement.
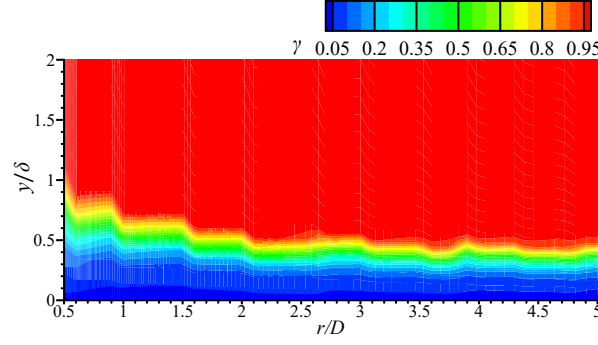
479

480   Figure 15. Development of γ in the radial direction for $H/D = 7$

481   Figure 16 depicts the γ gradient in the radial direction for different H/D. In the peak
482 mode, a laminar zone is clearly shown near the stagnation region, such as the case of
483 H/D=5. In the turbulence zone, γ is nearly in a steady state where the location of the
484 minimum gradient is almost at the same height. The occurrence of the minimum
485 gradient areas implies that the location is very near the turbulence edge, which can be
486 inferred from the case of H/D=7 (Figure 15 and Figure 16). However, near the
487 stagnation region, the positive radial gradient of γ deeply shows that the edge of
488 turbulence is developing. This phenomenon is much clearer in the peak mode, as shown
489 in Figure 16. The position for the end of the positive γ gradient ($P_{e\text{-}\gamma}$) seems to be
490 associated with impinging distance. When enhancing H/D in the peak mode, $P_{e\text{-}\gamma}$
491 moves forward to the stagnation point, meaning that the transition length becomes
492 shorter. Therefore, the secondary peak of Nu occurs earlier, as shown in Figure 11. In
493 the swelling mode, $P_{e\text{-}\gamma}$ exists before $r/D = 1.5$ when H/D≤6, indicating that the flow
494 quickly develops into the turbulent state in the transitional scope. However, beyond
495 H/D=6, the positive gradient disappears. It is emphasized that when the turbulence is
496 high enough, the laminar-turbulence transition is hard to occur. Figure 10 (a) shows
497 that the turbulent intensity is higher than 4.8% for H/D>6. Therefore, the change level
498 of intermittency is fairly mild in the whole plate compared with the peak and the
499 swelling modes. So the disappearance of the second peak of Nu can be explained
500 accordingly. In addition, in the following part, the laminar-turbulence transition process
501 will be analyzed quantitatively further.
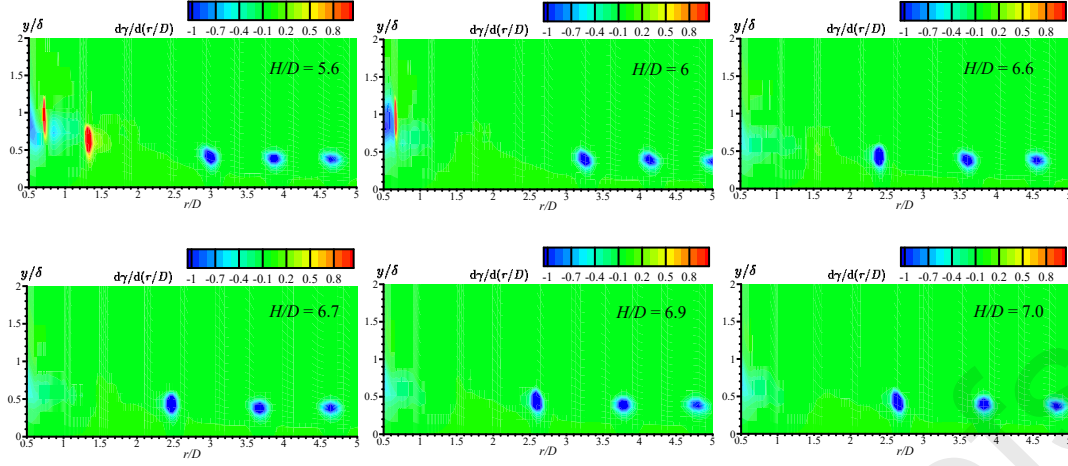
502

503

504

19
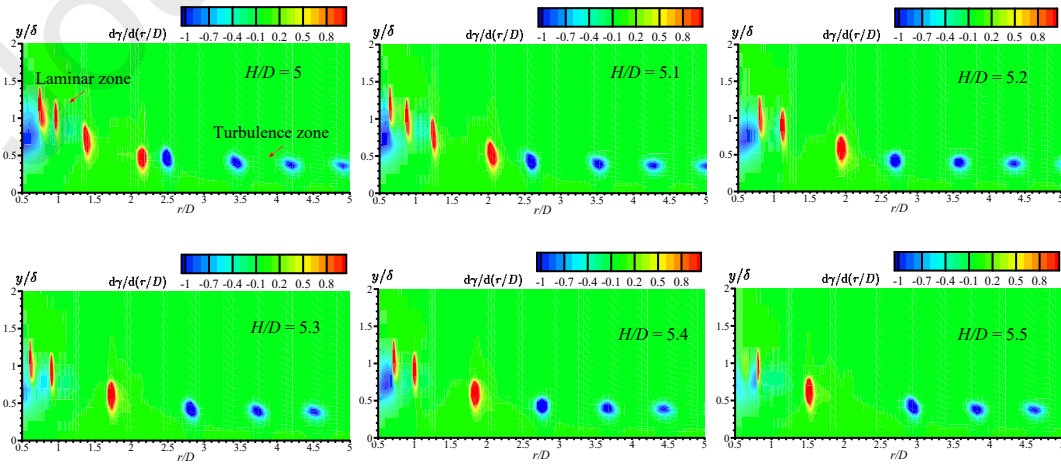
Figure 16. Development of γ in the boundary layer for different H/D

For the laminar-turbulence transition, another important issue stressed should be the skin friction coefficient C_f. This parameter plays an active role in the turbulent intensity so as to the heat transfer rate. Figure 17 (a) shows the SSTCDLM model's performance in predicting the skin friction coefficient at $H/D = 2$, which substantially agrees well with the experimental data. Two important characteristics are captured accurately by the SSTCDLM model. One is the maximum peak around $r/D = 0.5$ and the other is the local maximum around $r/D = 2$. However, in the peak mode referred in the paper, there is no local maximum peak around $r/D = 2$, as presented in Figure 17 (b). The maximum peak C_f reduces when increasing the nozzle-plate spacing around $r/D = 0.5$. Under the high nozzle-plate spacing condition, the jet width becomes wider, contributing to the lower maximum wall shear stress.

(a)   (b)
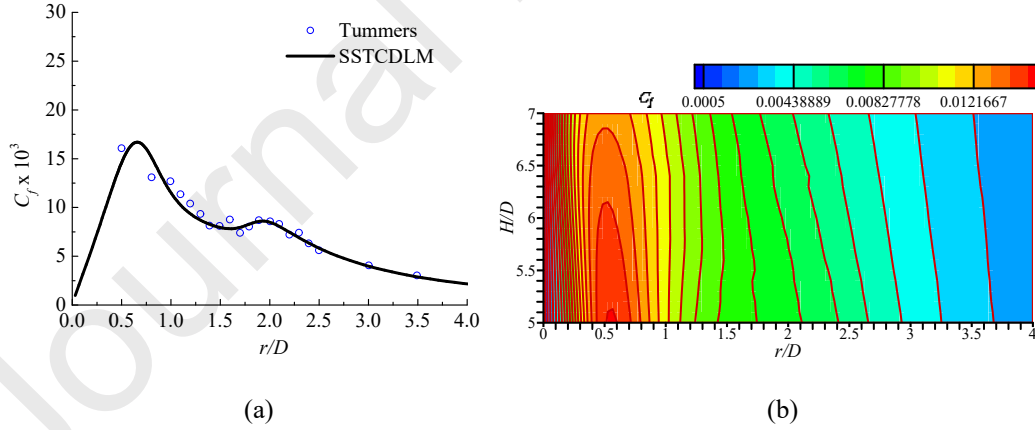
Figure 17. Skin friction coefficient C_f. (a) The numerical simulation results compared with the experimental data of Tummers et al. [22] at $H/D = 2$; and (b) The distributions along the impinging plate for different H/D

Although C_f does not show a similar mode compared with the heat transfer rate, the local skin friction coefficient C_{fl} still can gain insight into the contributions of laminar and turbulence. C_{fl} can be divided by

(24)

527 where the first term on the right-hand side is the laminar part based on the Blasius
528 boundary layer, the second term reflects the turbulence contribution, the third term is
529 associated with the streamwise growth of the angular momentum, the fourth term
530 denotes the mean wall-normal flux part, the fifth term reflects the influence of the
531 freestream pressure gradient, and the final term involves the effect of deviation from
532 the boundary layer approximation. Re_l can be computed by $Re_l = U_e l / v$. Different
533 boundary layer thicknesses can be defined as

$$\theta = \int_0^\infty \left(1 - \frac{u(y)}{U_e}\right)\frac{u(y)}{U_e}\,\mathrm{d}y \tag{25}$$

$$\delta^* = \int_0^\infty \left(1 - \frac{u(y)}{U_e}\right)\mathrm{d}y \tag{26}$$

$$\delta_l^* = \int_0^\infty \left(1 - \frac{y}{l}\right)\left(1 - \frac{u(y)}{U_e}\right)\mathrm{d}y \tag{27}$$

$$\theta_l = \int_0^\infty \left(1 - \frac{y}{l}\right)\left(1 - \frac{u(y)}{U_e}\right)\frac{u(y)}{U_e}\,\mathrm{d}y \tag{28}$$

$$\theta_v = \int_0^\infty \left(1 - \frac{u(y)}{U_e}\right)\frac{v(y)}{U_e}\,\mathrm{d}y \tag{29}$$

534 The characteristic length l is estimated by

$$l = \sqrt{vr/U_e} \tag{30}$$

535 It is to be noted that Eq. (24) is derived from the work of Elnahhas and Johnson [52]
536 based on a cylindrical coordinate with a very small rotation angle. Meanwhile, for jet
537 impingement, the free stream velocity is supposed to be the velocity at the edge of the
538 boundary layer U_e in Eqs. (24-30). Therefore, C_{fl} is written by

$$C_{fl} = \frac{\tau_w}{0.5\rho U_e^2} \tag{31}$$

539 To analyze the role of laminar and turbulence, the laminar and turbulence parts are
540 plotted in Figure 18. Note that only the cases of critical nozzle-plate spacing $H/D = 5.5$
541 and 6.6 are given here. Near the stagnation region, there is a negative sharp pressure
542 gradient and thus the fifth term in Eq. (24) is a positive non-zero value. But when the
543 wall jet is within the deceleration zone of $1 < r/D$, the above term changes to a
544 negative value. The flow deceleration and acceleration zones can be obtained from

Figure 7, which are almost the same for different H/D. Therefore, it can be found that the value of C_{fl} (represented by Total) is lower than the laminar part for $1 < r/D < 1.5$ for the case of $H/D = 5.5$. Near the stagnation point in the same case, the laminar values are lower than the values of C_{fl} due to the flow acceleration. In this case, the turbulence contribution to the wall shear stresses always keeps a low value in the scope of $r/D < 1$. Beyond $r/D = 1$, the turbulence part significantly increases, implying that the laminar-turbulence transition would be triggered downstream. When $r/D \geq 2.5$, the wall shear stresses are gradually dominated by the turbulence part. However at $H/D = 6.6$, the turbulence part at $r/D = 0.5$ reaches about 18% of the value of the turbulence part at $r/D = 8$, while it is only 7% in the case of $H/D = 5.5$. In addition, at the high nozzle-plate spacing, the influence of pressure gradient becomes weak due to a wide jet width. As a result, the laminar part is nearly identical to the total values within the region of $0 < r/D < 1.5$. The turbulence part begins to be higher than the laminar part at $r/D = 2$, which is earlier than that in the case of $H/D = 5.5$. Therefore, considering the above two factors, the laminar-turbulence transition process is difficult to occur in such a narrow region $(1.5 < r/D < 2)$. And this well explains why the mild change of radial gradient γ takes place in the stagnation at higher H/D, as shown in Figure 16.
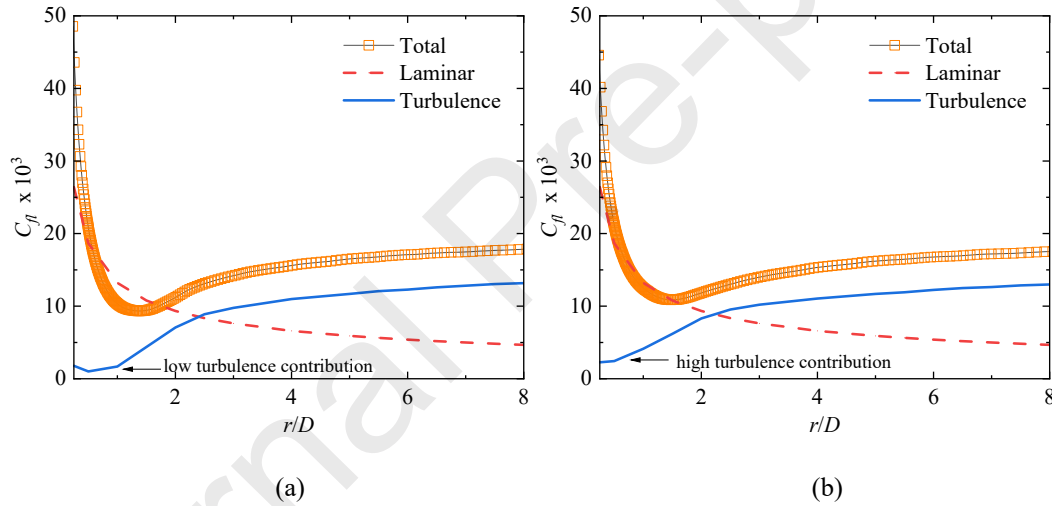

(a)   (b)

Figure 18. Different part of local skin friction coefficient C_{fl}. (a) $H/D = 5.5$ and (b) $H/D = 6.6$

4 Conclusions

In this paper, jet impingement heat transfer for different nozzle-plate spacing H/D with $Re = 23,000$ is investigated using the SSTCDLM model which is based on the SSTCD model and the SSTLM model. The transitional range of H/D is $5.5 \leq H/D \leq 6.6$, where the second peak of Nu gradually vanishes with increasing H/D. The SSTCDLM model shows superior performance in capturing the change of Nu. The transitional properties of heat transfer rate and flow behaviors at the stagnation point and transitional region are further discussed. The important conclusions are as follows:

(1) The SSTCD model fails to fit the measurement around the second peak of Nu and underpredicts the heat transfer rate downstream. For the SSTLM model, although the

577 second peak of Nu can be well reproduced, it usually overpredicts Nu at a high H/D
578 near the stagnation region. The predicted behavior of the SST model at high H/D is
579 almost identical to the SSTLM model. But at low nozzle-plate spacing, it cannot capture
580 the secondary peak of Nu. Fortunately, coupling the SSTCD and SSTLM models, the
581 SSTCDLM model is enable to regenerate the accurate occurrence and disappearance of
582 the secondary peak of Nu. The velocity field and the skin friction coefficient predicted
583 by the SSTCDLM model also match well with the experimental data.

584 (2) At the stagnation point, the heat transfer rate Nu_0 increases with H/D in the
585 above referred nozzle-plate spacing, which is due to the development of the potential
586 core as well as the turbulent intensity Tu. Meanwhile, it is found that $Nu_0/$
587 $\left(2\times(10Tu)^{1/5}\sqrt{Re_sPr}\right)$ almost keeps a constant. In the transitional region, the peak,
588 swelling, and linear modes appear sequentially, when the second peak of Nu gradually
589 disappears. By analyzing the radial gradient of Nu, two critical values of $H/D = 5.5$
590 and 6.6 are found, which can be used to characterize different modes. Meanwhile, for
591 $H/D < 5.5$, the maximum turbulent intensity Tu takes place in the transitional region,
592 while it moves forward to the stagnation region when the nozzle-plate spacing is
593 increased.

594 (3) The laminar-turbulence transition process is observed from the development of
595 the radial gradient of intermittency γ and the local skin friction coefficient C_{fl}. At H/D
596 = 5.5, a positive radial gradient of γ emerges around $r/D = 1$, for which the laminar part
597 of C_{fl} deviates from the total value. And the turbulence part of C_{fl} begins to increase
598 at the same location. This means that the laminar-turbulence transition takes place in
599 the peak mode. However, at $H/D = 6.6$, the laminar part of C_{fl} fits well with the total
600 value of C_{fl} up to $r/D = 1.5$, and the turbulence part of C_{fl} is fairly high in the stagnation
601 region. Due to the above two reasons, the effect of laminar-turbulence transition can be
602 ignored. Therefore, the change of radial gradient of γ becomes mild in the stagnation
603 region.

604

605 **Nomenclature**

C_f	Skin friction coefficient	r	Radial coordinate
C_{fl}	Local skin friction coefficient	p	Mean pressure
C_{p0}	Stagnation pressure coefficient	P_r	Prandtl number
c_p	Specific heat capacity at constant pressure	$P_{\theta t}$	Production term of $\widetilde{Re}_{\theta t}$
D	Nozzle diameter	P_γ	Transition production term

E_γ	Transition destruction term	S	Rate of strain tensor
F_1, F_2	Blending function	s	Arriving stream up to $y/D = 0.3$
H	Impinging distance	T	Temperature
h	Heat transfer coefficient	T_{in}	Temperature at the inlet
k	Turbulent kinetic energy	Tu	Turbulent intensity
k_{in}	Turbulent kinetic energy at the inlet	T_w	Temperature at the heated wall
l	Characteristic length	U_b	Bulk velocity
Nu	Nusselt number	U_{c0}	Centerline velocity at the nozzle exit
Nu_{avg}	Average Nusselt number	U_D	Mean uniform velocity at the nozzle inlet
Nu_0	Stagnation Nusselt number	U_e	Mean velocity at the edge of the boundary layer
Re	Inlet Reynolds number	U_{mag}	Mean velocity magnitude
Re_m	Reynolds number based on the centerline of free jet	u	Mean velocity
Re_s	Reynolds number based on the arriving stream	u_{in}	Mean velocity at the inlet
Re_l	Local Reynolds number	$\overline{u_i'u_j'}$	Reynolds stress
$\widetilde{Re}_{\theta t}$	Transition momentum-thickness Reynolds number	$\overline{u_i'T'}$	Turbulent heat flux vector
$P_{e\text{-}\gamma}$	End of the positive γ gradient	y	Vertical coordinate
y^+	Non-dimensional parameter for the first	y_f	Fully developed distance away

	grid distance to the wall		from the wall in y direction

Greek symbols

α_t	Turbulent thermal diffusivity	τ_w	Wall shear stress
δ	Boundary layer thickness	ρ	Density
δ^*	Displacement thickness	λ	Fluid thermal conductivity
δ_l^*	Length scale representing the first-order moments about l of the momentum deficit	μ	Dynamic viscosity
θ	Momentum thickness	ε	Dissipation rate
θ_l	Length scale representing the first-order moments about l of the momentum deficit fluxes	ω	Specific dissipation rate
θ_v	Length scale representing the integral of the vertical flux of streamwise momentum deficit	ω_{in}	Specific dissipation rate at the inlet
μ_t	Eddy viscosity	χ_k	Cross-diffusion factor
γ	Intermittency factor	χ_ω	Stretching factor
Ω	Rate of vorticity	γ_{eff}	Effective intermittency factor
$\mathcal{Z}_{r,\ell}$	Term involving the effect of deviation from the boundary layer approximation	v	Kinematic viscosity

606

Acknowledgements

613

Data Availability Statement

615 The datasets used and/or analyzed during the current study available from the
616 corresponding author on reasonable request.

617

Declaration of Competing Interest

619 The authors declare that there is no conflict of interest.

620

Reference

622 [1] N. Zuckerman, N. Lior, Jet impingement heat transfer: physics, correlations, and
623 numerical modeling, in: G.A. Greene, J.P. Hartnett†, A. Bar-Cohen, Y.I. Cho (Eds.),
624 Advances in Heat Transfer, Elsevier, 2006: pp. 565–631.
625 https://doi.org/10.1016/S0065-2717(06)39006-5.

626 [2] D. Edgington-Mitchell, Aeroacoustic resonance and self-excitation in screeching
627 and impinging supersonic jets – A review, International Journal of Aeroacoustics 18
628 (2019) 118–188. https://doi.org/10.1177/1475472X19834521.

629 [3] H. Li, Y. Luo, S. Han, Y. Wang, C. Wu, R. Ma, The source localization and
630 dynamical evolution of axisymmetric screech modes in underexpanded supersonic jets,
631 Aerospace Science and Technology 140 (2023) 108427.
632 https://doi.org/10.1016/j.ast.2023.108427.

633 [4] 覃晨, 岳廷瑞, 冯和英, 吴松岭, 曾波, 偏流板距离对亚声速射流冲击宽频噪
634 声特性的影响, 声学学报 48 (2023) 549–558. https://doi.org/10.15949/j.cnki.0371-
635 0025.2023.03.011.

636 [5] B. Markal, Experimental investigation of heat transfer characteristics and wall
637 pressure distribution of swirling coaxial confined impinging air jets, International
638 Journal of Heat and Mass Transfer 124 (2018) 517–532.
639 https://doi.org/10.1016/j.ijheatmasstransfer.2018.03.101.

640 [6] J. Inman, P. Danehy, R. Nowak, D. Alderfer, The effect of impingement on
641 transitional behavior in underexpanded jets, in: 47th AIAA Aerospace Sciences
642 Meeting Including The new horizons forum and aerospace exposition, American
643 Institute of Aeronautics and Astronautics, Orlando, Florida, 2009.
644 https://doi.org/10.2514/6.2009-591.

645 [7] A.M. Kuraan, S.I. Moldovan, K. Choo, Heat transfer and hydrodynamics of free
646 water jet impingement at low nozzle-to-plate spacings, International Journal of Heat
647 and Mass Transfer 108 (2017) 2211–2216.
648 https://doi.org/10.1016/j.ijheatmasstransfer.2017.01.084.

649 [8] D. Cooper, D.C. Jackson, B.E. Launder, G.X. Liao, Impinging jet studies for

turbulence model assessment—I. Flow-field experiments, International Journal of Heat and Mass Transfer 36 (1993) 2675–2684. https://doi.org/10.1016/S0017-9310(05)80204-2.

[9] J.W. Baughn, A.E. Hechanova, X. Yan, An Experimental study of entrainment effects on the heat transfer from a flat surface to a heated circular impinging jet, Journal of Heat Transfer 113 (1991) 1023–1025. https://doi.org/10.1115/1.2911197.

[10] M. Fénot, X.T. Trinh, E. Dorignac, Flow and heat transfer of a compressible impinging jet, International Journal of Thermal Sciences 136 (2019) 357–369. https://doi.org/10.1016/j.ijthermalsci.2018.10.035.

[11] A. Kumar, K. Yogi, S.V. Prabhu, Experimental and analytical study on local heat transfer distribution between smooth flat plate and free surface impinging jet from a circular straight pipe nozzle, International Journal of Heat and Mass Transfer 207 (2023) 124004. https://doi.org/10.1016/j.ijheatmasstransfer.2023.124004.

[12] S. Beltaos, N. Rajaratnam, Impingement of axisymmetric developing jets, Journal of Hydraulic Research 15 (1977) 311–326. https://doi.org/10.1080/00221687709499637.

[13] G. Zhang, H. Huang, T. Sun, N. Li, B. Zhou, Z. Sun, Analysis of the performance of a new developed shear stress transport model in a turbulent impinging jet flow, Physics of Fluids 31 (2019) 115110. https://doi.org/10.1063/1.5118675.

[14] J.E. Jaramillo, C.D. Pérez-Segarra, I. Rodriguez, A. Oliva, Numerical study of plane and round impinging jets using rans models, numerical heat transfer, Part B: Fundamentals 54 (2008) 213–237. https://doi.org/10.1080/10407790802289938.

[15] M. Hadžiabdić, K. Hanjalić, Vortical structures and heat transfer in a round impinging jet, Journal of Fluid Mechanics 596 (2008) 221–260. https://doi.org/10.1017/S002211200700955X.

[16] S.A. Salamah, D.A. Kaminski, Modeling of turbulent heat transfer from an array of submerged jets impinging on a solid surface, Numerical Heat Transfer, Part A: Applications 48 (2005) 315–337. https://doi.org/10.1080/10407780590945551.

[17] H. Huang, T. Sun, G. Zhang, M. Liu, Z. Zong, Analysis of the three-dimensional swirling and non-swirling jet impingement using a turbulence model with cross-diffusion correction, Applied Thermal Engineering 200 (2022) 117708. https://doi.org/10.1016/j.applthermaleng.2021.117708.

[18] M. Fenot, J.-J. Vullierme, E. Dorignac, Local heat transfer due to several configurations of circular air jets impinging on a flat plate with and without semi-confinement, International Journal of Thermal Sciences 44 (2005) 665–675. https://doi.org/10.1016/j.ijthermalsci.2004.12.002.

[19] T. Guo, M.J. Rau, P.P. Vlachos, S.V. Garimella, Axisymmetric wall jet development in confined jet impingement, Physics of Fluids 29 (2017) 025102. https://doi.org/10.1063/1.4975394.

[20] M. Shademan, R. Balachandar, V. Roussinova, R. Barron, Round impinging jets

690 with relatively large stand-off distance, Physics of Fluids 28 (2016) 075107.
691 https://doi.org/10.1063/1.4955167.

692 [21] J. Zhe, V. Modi, Near wall measurements for a turbulent impinging slot jet, journal
693 of fluids engineering 123 (2001) 112–120. https://doi.org/10.1115/1.1343085.

694 [22] M.J. Tummers, J. Jacobse, S.G.J. Voorbrood, Turbulent flow in the near field of a
695 round impinging jet, International Journal of Heat and Mass Transfer 54 (2011) 4939–
696 4948. https://doi.org/10.1016/j.ijheatmasstransfer.2011.07.007.

697 [23] F. Afroz, M.A.R. Sharif, Numerical study of turbulent annular impinging jet flow
698 and heat transfer from a flat surface, Applied Thermal Engineering 138 (2018) 154–
699 172. https://doi.org/10.1016/j.applthermaleng.2018.04.007.

700 [24] H. Huang, T. Sun, G. Zhang, M. Liu, B. Zhou, The effects of rough surfaces on
701 heat transfer and flow structures for turbulent round jet impingement, International
702 Journal of Thermal Sciences 166 (2021) 106982.
703 https://doi.org/10.1016/j.ijthermalsci.2021.106982.

704 [25] S. Abraham, R.P. Vedula, Effectiveness and heat transfer characteristics for a
705 single heated rectangular jet with different aspect ratios impinging perpendicularly on
706 a flat surface, International Journal of Heat and Mass Transfer 102 (2016) 1012–1023.
707 https://doi.org/10.1016/j.ijheatmasstransfer.2016.06.086.

708 [26] M.K. Isman, P.J. Morris, M. Can, Investigation of laminar to turbulent transition
709 phenomena effects on impingement heat transfer, Heat Mass Transfer 52 (2016) 2027–
710 2036. https://doi.org/10.1007/s00231-015-1719-8.

711 [27] R.B. Langtry, F.R. Menter, Correlation-based transition modeling for unstructured
712 parallelized computational fluid dynamics codes, AIAA Journal 47 (2009) 2894–2906.
713 https://doi.org/10.2514/1.42362.

714 [28] S. Alimohammadi, D.B. Murray, T. Persoons, Experimental validation of a
715 computational fluid dynamics methodology for transitional flow heat transfer
716 characteristics of a steady impinging jet, Journal of Heat Transfer 136 (2014) 091703.
717 https://doi.org/10.1115/1.4027840.

718 [29] A. Dewan, R. Dutta, B. Srinivasan, Recent trends in computation of turbulent jet
719 impingement heat transfer, Heat Transfer Engineering 33 (2012) 447–460.
720 https://doi.org/10.1080/01457632.2012.614154.

721 [30] T. Zhou, D. Xu, J. Chen, C. Cao, T. Ye, Numerical analysis of turbulent round jet
722 impingement heat transfer at high temperature difference, Applied Thermal
723 Engineering 100 (2016) 55–61. https://doi.org/10.1016/j.applthermaleng.2016.02.006.

724 [31] K.A. Ganatra, D. Singh, Comparison of Various RANS Models for Impinging
725 Round Jet Cooling From a Cylinder, Journal of Heat Transfer 141 (2019).
726 https://doi.org/10.1115/1.4043304.

727 [32] J. Wu, H. Xiao, R. Sun, Q. Wang, Reynolds-averaged Navier–Stokes equations
728 with explicit data-driven Reynolds stress closure can be ill-conditioned, J. Fluid Mech.
729 869 (2019) 553–586. https://doi.org/10.1017/jfm.2019.205.

[33] J. Ortega-Casanova, F. Molina-Gonzalez, Axisymmetric numerical investigation of the heat transfer enhancement from a heated plate to an impinging turbulent axial jet via small vortex generators, International Journal of Heat and Mass Transfer 106 (2017) 183–194. https://doi.org/10.1016/j.ijheatmasstransfer.2016.10.064.

[34] Z.U. Ahmed, Y.M. Al-Abdeli, F.G. Guzzomi, Flow field and thermal behaviour in swirling and non-swirling turbulent impinging jets, International Journal of Thermal Sciences 114 (2017) 241–256. https://doi.org/10.1016/j.ijthermalsci.2016.12.013.

[35] X. Kong, Y. Zhang, G. Li, X. Lu, J. Zhu, J. Xu, Simulation on the effect of impinging distance for the aerodynamic and heat transfer characteristics of sweeping jet and film composite cooling, Applied Thermal Engineering 227 (2023) 120382. https://doi.org/10.1016/j.applthermaleng.2023.120382.

[36] V.K.S. Chauhan, K. Kumari, P. Kumar, V.K. Venkiteswaran, M.M. Awad, Numerical study of eccentric jet impingement cooling on a heated cylindrical surface, ASME Journal of Heat and Mass Transfer 146 (2024). https://doi.org/10.1115/1.4064456.

[37] R. Dutta, A. Dewan, B. Srinivasan, Comparison of various integration to wall (ITW) RANS models for predicting turbulent slot jet impingement heat transfer, International Journal of Heat and Mass Transfer 65 (2013) 750–764. https://doi.org/10.1016/j.ijheatmasstransfer.2013.06.056.

[38] H. Huang, T. Sun, G. Zhang, D. Li, H. Wei, Evaluation of a developed SST k-w turbulence model for the prediction of turbulent slot jet impingement heat transfer, International Journal of Heat and Mass Transfer 139 (2019) 700–712. https://doi.org/10.1016/j.ijheatmasstransfer.2019.05.058.

[39] F.S. Alvi, J.A. Ladd, W.W. Bower, Experimental and computational investigation of supersonic impinging jets, AIAA Journal 40 (2002) 599–609. https://doi.org/10.2514/2.1709.

[40] R. Vinze, A. Khade, P. Kuntikana, M. Ravitej, B. Suresh, V. Kesavan, S.V. Prabhu, Effect of dimple pitch and depth on jet impingement heat transfer over dimpled surface impinged by multiple jets, International Journal of Thermal Sciences 145 (2019) 105974. https://doi.org/10.1016/j.ijthermalsci.2019.105974.

[41] Z.U. Ahmed, Y.M. Al-Abdeli, F.G. Guzzomi, Impingement pressure characteristics of swirling and non-swirling turbulent jets, Experimental Thermal and Fluid Science 68 (2015) 722–732. https://doi.org/10.1016/j.expthermflusci.2015.07.017.

[42] OpenFOAM-10, The OpenFOAM Foundation Ltd Incorporated, https://openfoam.org/.

[43] F.R. Menter, M. Kuntz, R. Langtry, Ten years of industrial experience with the SST turbulence model, Heat and Mass Transfer (n.d.).

[44] J.W. Baughn, S. Shimizu, Heat transfer measurements from a surface with uniform heat flux and an impinging jet, Journal of Heat Transfer 111 (1989) 1096–1098. https://doi.org/10.1115/1.3250776.

[45] J.W. Baughn, X.J. Yan, M. Mesbah, The effect of Reynolds number on the heat transfer distribution from a flat plate to a turbulent impinging jet, in: ASME, Anaheim, California, 1992.

[46] C. He, Y. Liu, A dynamic detached-eddy simulation model for turbulent heat transfer: Impinging jet, International Journal of Heat and Mass Transfer 127 (2018) 326–338. https://doi.org/10.1016/j.ijheatmasstransfer.2018.06.117.

[47] D.H. Lee, J. Song, M.C. Jo, The effects of nozzle diameter on impinging jet heat transfer and fluid flow, Journal of Heat Transfer 126 (2004) 554–557. https://doi.org/10.1115/1.1777583.

[48] C.J. Hoogendoorn, The effect of turbulence on heat transfer at a stagnation point, International Journal of Heat and Mass Transfer 20 (1977) 1333–1338. https://doi.org/10.1016/0017-9310(77)90029-1.

[49] K. Kataoka, R. Sahara, H. Ase, T. Harada, Role of large-scale coherent structures in impinging jet heat transfer., Journal of Chemical Engineering of Japan 20 (1987) 71–76. https://doi.org/10.1252/jcej.20.71.

[50] Z.U. Ahmed, Y.M. Al-Abdeli, F.G. Guzzomi, Impingement pressure characteristics of swirling and non-swirling turbulent jets, Experimental Thermal and Fluid Science 68 (2015) 722–732. https://doi.org/10.1016/j.expthermflusci.2015.07.017.

[51] A.A. Tawfek, Heat transfer and pressure distributions of an impinging jet on a flat surface, Heat and Mass Transfer 32 (1996) 49–54. https://doi.org/10.1007/s002310050090.

[52] A. Elnahhas, P.L. Johnson, On the enhancement of boundary layer skin friction by turbulence: an angular momentum approach, Journal of Fluid Mechanics 940 (2022) A36. https://doi.org/10.1017/jfm.2022.264.

Highlights

(1) A coupled method of the SSTCDLM is developed and investigated for jet impingement.

(2) The transitional impinging type is studied in flow fields and heat transfer.

(3) The laminar-turbulence transition process is presented in details.

(4) The peak, swelling and linear modes are found in the transitional type.

(5) The contribution of the laminar and turbulence to the flow is discussed.

30